Spaceborne GNSS-R Minimum Variance Wind Speed Estimator

Maria Paola Clarizia, Christopher S. Ruf, *Fellow, IEEE*, Philip Jales, and Christine Gommenginger

***Abstract*—A Minimum Variance (MV) wind speed estimator for Global Navigation Satellite System-Reflectometry (GNSS-R) is presented. The MV estimator is a composite of wind estimates obtained from five different observables derived from GNSS-R Delay-Doppler Maps (DDMs). Regression-based wind retrievals are developed for each individual observable using empirical geophysical model functions that are derived from NDBC buoy wind matchups with collocated overpass measurements made by the GNSS-R sensor on the United Kingdom-Disaster Monitoring Constellation (UK-DMC) satellite. The MV estimator exploits the partial decorrelation that is present between residual errors in the five individual wind retrievals. In particular, the RMS error in the MV estimator, at 1.65 m/s, is lower than that of each of the individual retrievals. Although they are derived from the same DDM, the partial decorrelation between their retrieval errors demonstrates that there is some unique information contained in them. The MV estimator is applied here to UK-DMC data, but it can be easily adapted to retrieve wind speed for forthcoming GNSS-R missions, including the UK's TechDemoSat-1 (TDS-1) and NASA's Cyclone Global Navigation Satellite System (CYGNSS).**

***Index Terms*—Delay-Doppler map, global navigation satellite systems (GNSS)-reflectometry, minimum variance (MV) estimator, ocean surface wind speed.**

I. Introduction and Background

THE ocean surface wind is a crucial parameter that affects maritime operations and ship routing, determines the energy exchange at the air-sea interface, and influences the ocean circulation and climate in general. Surface winds also have a strong influence on the genesis, development and intensification of extreme events like Tropical Cyclones (TC) or hurricanes. For all these reasons, it is important to monitor the ocean surface wind on a global basis for operational oceanography, climate studies, and weather forecasting.

While *in situ* instruments like buoys and ships provide near-continuous measurements of the surface wind vector, their spatial sampling is insufficient to provide a global and synoptic map of surface winds. Global coverage with adequate temporal resolution can only be achieved through the use of satellites and, in particular, through sensors operating at microwave frequencies, that can measure the surface wind vector day and night, and can penetrate through clouds and rain (provided the wavelength is long enough). Scatterometers [1]–[7], Radar Altimeters [8]–[10] and Synthetic Aperture Radar (SAR) [11]–[13] are all active radar sensors with the capability of measuring sea surface wind speed. Scatterometers in particular, like QuikScat, ASCAT and OSCAT, are specifically designed to measure near-surface winds over the ocean by measuring the backscattered radar cross section and relating it to the wind speed - usually through an empirical Geophysical Model Function (GMF) [14]–[17]. They typically operate in the 2–5 cm range of wavelengths, which makes the radar backscatter very sensitive to small-scale capillary waves generated by the wind, but also makes more challenging the retrieval in heavy precipitation conditions, such as those experienced during TCs. Radar altimeters are also used for wind speed retrieval, although they have much more limited spatial coverage than wide-swath imaging scatterometers [8]–[10]. SAR can provide wind measurements at high spatial resolution, and, for those operating at suitable wavelengths, even in the presence of rain [11]–[13]. Wind speed measurements are also obtained by passive microwave radiometers, through measurement of the excess surface emissivity caused by surface roughness and foam [18], [19].

GNSS-Reflectometry (GNSS-R) is a relatively new remote sensing technique which exploits pre-existing signals of opportunity transmitted by Global Navigation Satellite Systems (GNSS) such as the GPS, Galileo and GLONASS constellations to form a bistatic radar [20]–[40]. The direct signal is received through a zenith antenna, to pin-point the position of the transmitting and receiving satellites and to provide a timing reference, and the signal scattered from the surface of the ocean is received through a downward pointing antenna. The scattered signal contains detailed information about the ocean surface roughness statistics, from which local wind speed can be retrieved [25], [30], [37].

The main advantages of GNSS-R lie in the global availability of GNSS signals, which provides a dense coverage over the Earth and offers the potential for significant improvements in spatio-temporal sampling of the ocean winds and waves. The receiver needed to capture the surface reflections is small and cheap, low-weight/low-power, and can be easily accommodated on small satellites or satellites of opportunity, thus reducing the cost of a mission and allowing for constellations of multiple GNSS-R receivers. As a final remark, GNSS signals operate at L-band. Their longer wavelength than traditional ocean wind

Manuscript received August 31, 2013; revised December 13, 2013; accepted January 25, 2014. Date of publication February 19, 2014.

M. P. Clarizia is with the Atmospheric, Oceanic and Space Sciences (AOSS), University of Michigan, Ann Arbor, MI 48109-2143 USA and also with the National Oceanography Centre, SO14 3ZH Southampton, U.K.

C. S. Ruf is with the Atmospheric, Oceanic and Space Sciences (AOSS), University of Michigan, Ann Arbor, MI 48109-2143 USA.

P. Jales is with the Surrey Satellite Technology Ltd., GU2 7YE Guildford, U.K.

C. Gommenginger is with the National Oceanography Centre, SO14 3ZH Southampton, U.K.

Color versions of one or more of the figures in this paper are available online at http://ieeexplore.ieee.org.

Digital Object Identifier 10.1109/TGRS.2014.2303831

0196-2892 © 2014 IEEE. Personal use is permitted, but republication/redistribution requires IEEE permission.
See http://www.ieee.org/publications_standards/publications/rights/index.html for more information.

scatterometers is advantageous for observations through heavy precipitation, which has only a minor effect. This makes them particularly well suited for observing phenomena such as tropical cyclones [41], [42]. Scattering from the ocean at longer wavelengths is influenced by both the smaller capillary waves that are well coupled to local winds, and by longer (e.g., swell) waves which are less so. This can introduce some decorrelation between variations in the scattered signal at L-band and the local wind field.

GNSS-R measurements are usually processed into the form of so-called Delay-Doppler Maps (DDMs), which are 2-D maps of scattered power from the surface as a function of the difference in propagation time and Doppler shift of the scattered signal relative to the direct signal. DDMs are formed through a cross-correlation of the received scattered signal with a locally generated and time-synchronized replica of the C/A code of the transmitted signal, for varying delay-Doppler coordinates [28]. Such cross-correlation is usually done over 1 ms, and is heavily affected by speckle noise, so that a large number of incoherent accumulations of consecutive cross-correlation values is necessary to mitigate the noise. The typical incoherent accumulation time for spaceborne DDMs is 1 second [30]. DDMs typically exhibit a distinctive horseshoe-like shape due to the space-to-DD coordinate transformation and consequent reshaping of the spatial distribution of scattered power. A prominent maximum at the apex of the horseshoe represents the power scattered from the specular reflection point (SP), and the extremities of the horseshoe shape represent the power scattered from the area surrounding the SP, referred to as the glistening zone. In general, stronger winds tend to decrease the power near the SP in the DDM and increase the extent of the glistening zone [37]. GNSS-R works in a regime of forward specular reflection, which has a complementary behavior with respect to backscattering, since the strongest reflection occurs at low winds, whereas the backscattered power tends to increase with increasing winds.

In the last 20 years, a number of airborne campaigns and ground-based platforms have successfully been deployed to acquire GNSS-R signals scattered from the ocean surface [21]–[23], [26], [27], [29], [31], [40]. The first spaceborne GNSS-R measurements were made in 2000 onboard the space shuttle SIR-C, but at a relatively low altitude of about 200 km [24]. The GNSS-R experiment carried onboard the Surrey Satellite Technology Ltd (SSTL) UK-DMC satellite [43], is recognized as the first experiment to successfully measure and process a number of surface scattered signals [28], [30], [33], [37]–[39]. The UK-DMC satellite was decommissioned in 2011, but a number of new spaceborne GNSS-R missions are expected to launch in the near future. The most important ones are: a) the UK TechDemoSat-1 (TDS-1) [44], [45], due to be launched in late 2013, which will provide a spaceborne platform for the demonstration of several new instrument concepts, and will host the next generation of SSTL's GPS-Reflectometry Receiver (called SGR-ReSI), and b) The NASA CYclone Global Navigation Satellite System (CYGNSS) Earth Venture mission, made up of a constellation of 8 microsatellites, which aims to measure sea surface winds in Tropical Cyclones (TC) and hurricanes, with a particular focus on their inner core [41], [42].

II. UK-DMC Experiment

The UK-DMC satellite, launched in 2003, was placed in a sun-synchronous orbit with an altitude of $\sim$680 km. The GNSS-R experiment, which shared the platform with a number of other instruments, lead to about 50 measurements of scattering from the ocean surface, plus a number of additional measurements over land, snow and ice [28], [30], [39], [43].

The payload for the GNSS bistatic experiment was made up of a GPS receiver, a solid state data recorder and an additional downward pointing antenna, which was added to the two standard space pointing (zenith) antennas. The downward pointing antenna had a peak gain of 11.8 dBi and was tuned to capture the GPS signal on the L1 carrier at 1575 MHz. The zenith antenna is Right Hand Circularly Polarized to capture the direct GPS signal; the nadir antenna is Left Hand Circularly Polarized (LHCP), since the transmitted signal reverses its polarization when scattered by the sea surface [46]. The nadir antenna's 3 dB footprint is 28° along track and 70° cross track, covering an area of about 200×1000 km^2. The nominal orientation for the antenna was 10° behind the satellite, although in some cases the antenna was oriented in a different way to accommodate specific requests to target given areas for acquisition. The solid state data recorder performed raw data sampling of the down-converted signals from both the zenith and nadir antennas, and was able to store up to 20 seconds of continuous data. The Intermediate Frequency (IF) raw sampled data were recorded on-board by a solid state data recorder and then telemetered to the ground for post-processing to generate the DDMs [28], [30].

The UK-DMC mission collected more than 60 GPS-R acquisitions, mainly around the US coast (Hawaii, Alaska, Gulf Stream region) over a period of several months between 2004 and 2005, but with some later data-sets up until 2011, when UK-DMC was taken out of service. Approximately 50 GPS-R acquisitions over various types of surfaces were obtained over the ocean, $\sim$30 of which were programmed to be located within 100 km and 1 hour of meteorological and wave buoy stations by U.S. National Data Buoy Center (NDBC). NDBC buoys are capable of measuring wind speeds over a dynamic range of 0 m/s to 62 m/s, with a resolution of 0.1 m/s, and with an accuracy that depends on the type of payload on the buoy, usually being either 1 m/s or the greater of 1 m/s and 10% of the measured winds [52].

Each acquisition contains reflections from different GPS satellites (PRNs) occurring simultaneously in different directions with respect to the receiver, making a total of $\sim$300 reflections. Each reflection is made up of 13–19 seconds of raw data, and for this reason we also call it a raw data stream. The raw data stream is subsequently processed to produce a DDM stream, with one DDM every 1 second. A few recent studies have highlighted the possibility to retrieve wind [28], [30], [38] and Directional Mean Square Slopes (DMSS) [33] using UK-DMC data. These studies show overall good agreement with collocated information from the NDBC buoys.

The entire set of UK-DMC GPS-R acquisitions has recently been processed and catalogued, using improved and advanced signal processing methods [39]. In this paper, a number of these acquisitions have been selected, based on spatio-temporal collocation with NDBC buoy ground-truth wind speed

measurements, and forming the UK-DMC data set used for this study. Five versions of a wind speed retrieval algorithm have been applied to the data set, based on five different quantities derived from the DDMs, referred to as DDM observables. The wind estimates from these observables are combined together by a Minimum Variance (MV) wind speed estimator, which is shown to deliver improved wind speed retrieval performances relative to each individual observables.

III. Description of Spaceborne Data Set

The UK-DMC data set used for this study consists of 29 collocated NDBC buoy overpasses, where each overpass consists of a 13–19 second raw data stream and an NDBC buoy measurement. The spatio/temporal collocation criteria adopted for this selection were 100 km maximum spatial distance between the buoy and the SP, and 1 hour maximum temporal distance between the buoy and UK-DMC acquisition. These collocation criteria are typical of those used to validate satellite wind and wave measurements where wind and sea state can change rapidly both in space and time [10]. Table I shows the information about each UK-DMC overpass, along with all the relevant buoy information. The buoy-measured wind speed is extracted from the historical standard meteorological database from the NDBC website, where an average wind speed value is reported every hour.

The DDMs generated for this study were formed from the combination of two processes, tracking the SP and then measuring the signal power as a DDM around this point. The full description of this process is contained in [39] and here the outline of the approach is given.

The processing tool used to produce the DDMs is based on a software-defined radio GNSS receiver extended for GNSS reflectometry. This tracks the reflection by calculating an estimate of the SP delay and Doppler from the transmitter, receiver positions and the earth geoid. This is open-loop so the prediction is not updated by measurements of the resulting DDM which avoids introducing tracking offsets due to noise in the DDM.

The process flow, shown in Fig. 1, starts with raw samples from the zenith antenna, which use the standard GNSS receiver techniques of acquisition followed by signal tracking. The navigation solution is formed from the tracking pseudoranges and the GPS transmitter ephemerides. The UK-DMC data sets are too short to contain sufficient sub-frames in the navigation message so the ephemerides are provided as an additional input.

The navigation solution results in the positions and velocities of the transmitters and receiver. Then for each transmitter the SP location is calculated on the Earth's surface, which is modeled as a geoid with undulations as an approximation for the true sea surface. The propagation delay is calculated from the path: transmitter to SP to receiver. The Doppler is calculated from the rate of change of this path. These path delay and Doppler estimates are passed to the open-loop correlators as carrier frequency, code frequency and code phase to center the DDM on the SP. The software receiver time-synchronizes the raw samples at the first sub-frame in the broadcast data message. This results in the DDM processing starting from a maximum of 6 seconds into the start of the collection.

Following the tracking the DDM processing is performed. Each DDM pixel is the result of a matched filter of the raw samples by the GPS L1 C/A signal offset from the SP code delay and carrier frequency. The calculation for a single pixel is shown diagrammatically in Fig. 2. Following coherent matched filtering, the incoherent sum is performed to average the noise from the weak and relatively incoherent reflections and reduce speckle noise. This calculation approach is computationally intensive as each pixel requires the replication of these calculations. The DDMs were instead processed in the frequency domain to reduce computational complexity and to provide similarity to the approach to be performed in real-time on the TDS-1 and CYGNSS GNSS-R receivers.

The processing approach described in [39] is performed such that the Doppler pixels are calculated through spectrum estimation computed by Fourier transform. In Fig. 3 the process is shown, firstly the carrier of the specular path is removed through a down-conversion such that 0 Hz corresponds to the Doppler of the specular path. This is followed by a set of delay-channels that multiply the signal by the C/A code with delay spaced to provide a resolution of 0.2 chips between DDM rows. Each of these delay-channels then has a demodulated signal at a small range of residual Doppler that corresponds to the spread from the sea surface.

To reduce the computational complexity of the spectrum estimation stage, the signals are filtered and down-sampled to reduce the bandwidth of the calculated DDM. In this case the filtering is provided by a first-order Cascaded Integrator Comb filter and the decimation reduces the sample rate from 5.71 MHz to 32 kHz. A 1 ms coherent integration is formed by taking 32 of the decimated samples. Then the Fourier transform is over-sampled by zero-padding the input to make up a 4 ms block of samples, resulting in 250 Hz resolution. Each coherent DDM is then incoherently accumulated for either 50 milliseconds or 1 second, depending on the requirements of the DDM observable (see Section IV).

Some of the 29 overpasses were filtered out from the analysis by quality control tests. The buoys for two overpasses had missing wind speed values at the time of the UK-DMC acquisition, so those overpasses were removed. The spatial uniformity of the wind field during each overpass was used as a second filter, so that the differences in time and space sampling between the buoy and satellite would not introduce significant errors. The uniformity was tested by examining the time dependence of the GPS-R measurements during each overpass. In particular, the average scattered power in the near vicinity of the SP, referred to as the Delay-Doppler Map Average, or DDMA (see Section IV-A for an exact definition), was examined and overpasses for which the DDMA was not reasonably constant were removed. Fig. 4 shows the DDMA time series for each of the 27 overpasses with collocated buoy data. Three of the 27 overpasses (overpasses A, B and C) were removed for wind non-uniformity. Fig. 4 also highlights one case (labeled as D) in which the wind speed is no longer uniform after the 15th second of the time series. For this reason, we truncate this raw data stream after 15 seconds. A final two overpasses were filtered out which had the highest and lowest values of wind speed of the remaining overpasses. They were removed to reduce the

TABLE I
OVERPASS DETAILS OF UK-DMC DATA SET USED FOR THIS ANALYSIS, TOGETHER WITH INFORMATION FROM COLLOCATED NDBC BUOYS. THE LABELS "LATstart/LONstart" AND "LATend/LONend" INDICATE THE LATITUDE/LONGITUDE, RESPECTIVELY, OF THE INITIAL AND FINAL SP OF EACH DATA SET

ID/ PRN	TIME [dd/mm/yy hh:mm]	LAT_{start} [°]	LON_{start} [°]	LAT_{end} [°]	LON_{end} [°]	BUOY ID	PEAK TO NOISE RATIO	BUOY TIME [dd/mm/yy hh:mm]	BUOY LAT [°]	BUOY LON [°]	BUOY U10 [m/s]
R12/ 15	16/11/2204 07:55	41.09	-136.40	40.35	-136.64	46006	1.61	16/11/2204 08:00	40.84	-137.48	**8.3**
R12/ 21	16:11:2004 07:55	38.78	-128.75	38.04	-129.04	46059	1.27	16:11:2004 08:00	37.98	-129.99	**6.3**
R12/ 22	16/11/2004 07:55	41.02	-137.87	40.29	-138.10	46006	1.63	16/11/2004 08:00	40.84	-137.48	**8.3**
R13/ 22	26/11/2004 07:36	45.66	-131.46	44.93	-131.72	46005	2.22	26/11/2004 08:00	46.06	-131.01	**2.4**
R15/ 13	30/01/2005 09:05	23.10	-161.86	22.17	-162.08	51001	1.50	30/01/2005 09:00	23.43	-162.20	**7.4**
R20/ 13	21/03/2005 07:30	42.27	-130.96	41.52	-131.19	46002	1.74	21/03/2005 07:00	42.52	-130.26	**3.6**
R21/ 29	02/05/2005 09:16	23.75	-162.14	22.77	-162.37	51001	1.64	02/05/2005 09:00	23.43	-162.20	**5.2**
R22/ 26	17/05/2005 08:50	17.34	-157.83	16.47	-158.02	51002	1.59	17/05/2005 09:00	17.19	-157.82	**10.4**
R30/ 5	24/06/2005 09:29	52.78	-156.16	51.94	-156.57	46066	1.53	24/06/2005 09:00	52.69	-154.98	**6.7**
R33/ 6	24/07/2005 08:44	17.10	-158.76	16.27	-158.95	51002	1.37	24/07/2005 09:00	17.19	-157.82	**9.3**
R37/ 21	02/09/2005 08:57	56.41	-147.97	55.69	-148.36	46001	1.15	02/09/2005 09:00	56.29	-148.17	**6.6**
R40/ 22	26/09/2005 09:21	23.02	-161.99	22.39	-162.15	51001	2.70	26/09/2005 09:00	23.43	-162.20	**3.6**
R46/ 10	24/10/2005 03:51	30.14	-80.54	29.40	-80.73	41012	1.60	24/10/2005 04:00	30.08	-80.50	**7.9**
R47/ 19	12/11/2005 09:11	23.67	-161.69	22.81	-161.89	51001	1.12	12/11/2005 09:00	23.43	-162.20	**7.0**
R48/ 5	18/11/2005 20:42	50.47	-177.45	51.28	-178.02	46071	1.47	18/11/2005 21:00	51.17	-179.00	**8.5**
R50/ 9	21/11/2005 20:56	54.46	-172.57	55.39	-173.04	46073	1.36	21/11/2005 21:00	54.94	-172.02	**9.8**
R51/ 20	23/11/2005 10:59	57.11	-176.55	56.39	-176.98	46035	1.36	23/11/2005 11:00	56.91	-177.81	**6.2**
R57/ 5	09/12/2005 20:42	54.81	-172.29	55.43	-172.65	46073	1.55	09/12/2005 21:00	54.94	-172.02	**10.7**
R10/ 17	03/09/2004 07:25	37.25	-130.36	36.52	-130.59	46059	1.56	03/09/2004 07:00	37.98	-129.99	**10.2**
R31/ 5	07/07/2005 09:33	23.54	-162.06	22.69	-162.24	51001	1.47	07/07/2005 10:00	23.43	-162.20	**8.9**
R52/ 5	24/11/2005 21:09	50.27	-178.48	51.20	-178.96	46071	2.22	24/11/2005 21:00	51.17	-179.00	**7.6**
R52/ 9	24/11/2005 21:09	51.15	-172.89	52.09	-173.25	46072	1.51	24/11/2005 21:00	52.02	-172.10	**5.2**

uncertainty in the relationship between scattered power and measured DDM caused by the Automatic Gain Control (AGC) circuitry in the GPS receiver. The effects of AGC signal conditioning are largest at the highest and lowest winds. This is corroborated by the fact that, when these two overpasses were included, they exhibited the two largest wind retrieval errors. The total number of UK-DMC overpasses used for the retrieval algorithms presented in the next section was reduced from 29 to 22.

IV. WIND SPEED RETRIEVAL ALGORITHMS FROM SURFACE SCATTERING OBSERVABLES

Five wind speed retrieval algorithms are developed, based on different quantities derived from the DDMs. We refer to them as DDM observables. The observables include the Delay-Doppler Map Average (DDMA), the Delay-Doppler Map Variance (DDMV), Allan Delay-Doppler Map Variance (ADDMV), Leading Edge Slope (LES), and Trailing Edge Slope (TES).

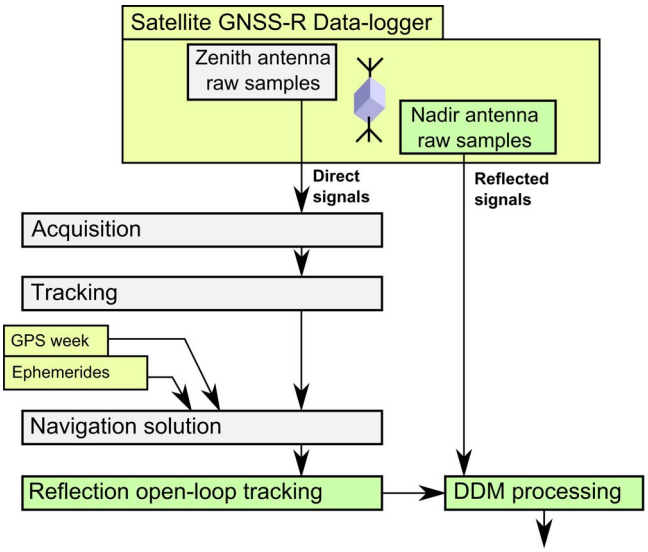


Fig. 1. Data flow for processing DDM stream aligned by open-loop tracking.

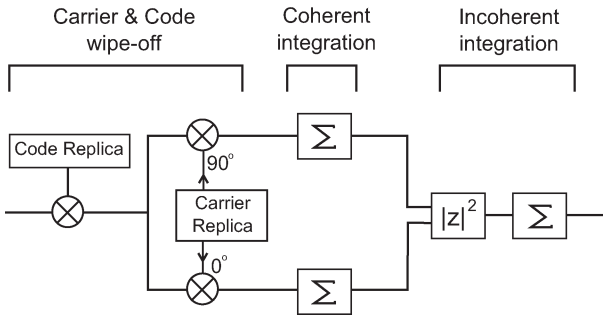


Fig. 2. Single pixel of a DDM, using the time-domain approach.

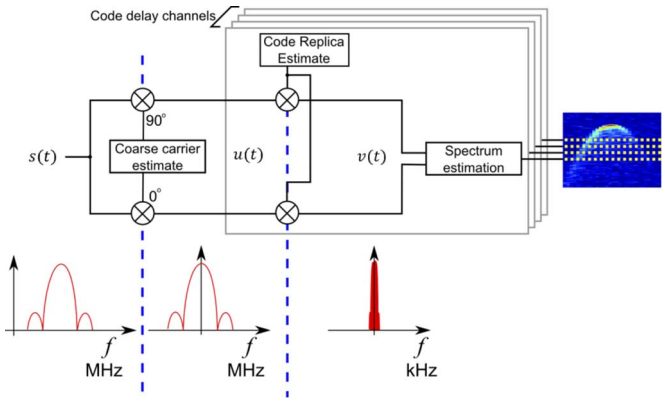


Fig. 3. Computation of DDM row through the process of downconversion, demodulation, and followed by spectrum estimation.

Each of these observable is introduced here for the first time as a means of extracting wind speed information from the DDMs. One observable that has been used previously, the DDM Volume [32], considers the spatial extent of the spread in forward diffuse scattering due to ocean roughness, and has been used to extrapolate wind and wave information from GNSS-R data, both from fixed platforms [35] and from aircraft [40]. The DDM Volume is not considered here due to our interest in limiting the spatial extent of the region over which the DDM is examined, which determines the spatial resolution of the retrieved wind speed.

In each case, the retrieval algorithms follow a common statistical inversion approach that uses an empirical GMF derived from NDBC buoy wind matchups against their respective DDM observable. The steps taken to develop each retrieval algorithm are as follows:

a) All available DDM observables and collocated buoy winds are assembled;
b) An empirical GMF is constructed from the matchups using least squares regression analysis;
c) The GMF is used as the basis for the mapping from DDM observable to estimated wind speed;
d) The Root Mean Square (RMS) difference between the estimated wind and the NDBC ground truth wind speed is computed as the RMS error in the retrieval.

This type of wind retrieval algorithm is often used in scatterometry [47] and SAR [48], where empirical GMFs are derived from a large collocation study between observed scatterometer backscatter measurements together with *in situ* buoy and/or Numerical Weather Prediction model data. In our case, the retrieval algorithms are demonstrated using a small data set of wind matchups, since only a handful of UK-DMC GPS-R acquisitions were collocated with NDBC buoys. Future GNSS-R missions (like CYGNSS) will make use of a large data set of collocated wind speed information from different sources (including buoys, model outputs, aircraft measurements and satellite cross-overs) which will help construct a robust empirical GMF model for each observable.

In the subsections that follow, we provide the definition and description of 5 observables derived from DDMs, and implement and apply the described retrieval algorithm to each of them.

A. Delay-Doppler Map Average (DDMA)

The Delay-Doppler Map Average (DDMA) is the average scattered power computed over a specified delay-Doppler window of the DDM around the SP. The DDMA can be written as

$$\mathrm{DDMA}_Y(\Delta\tau, \Delta f, t_i) = \frac{1}{MN} \sum_{m=1}^{M} \sum_{n=1}^{N} \overline{Y}(t_m, f_n, t_i) \quad (4.1)$$

where $\Delta\tau = \tau_M - \tau_1$ and $\Delta f = f_N - f_1$ are, respectively the delay and Doppler ranges over which to compute the DDMA, and $\overline{Y}(\tau_m, f_n, t_i)$ is the scattered power value minus the noise floor, at the delay and Doppler coordinates τ_m and f_n, of the 1-second DDM at time τ_i. The delay, Doppler and time coordinates are in this case all discrete quantities. The DDMA exploits the region in the DDM that is most sensitive to varying wind speed, namely the scattered power at and around the SP (see Fig. 5).

Two important parameters that characterizes the DDMA, as well as the other observables described below, are:

a) The location of the SP in the DDM, to be used as the center for DDMA calculation;
b) The delay and Doppler ranges over which to average the DDMA.

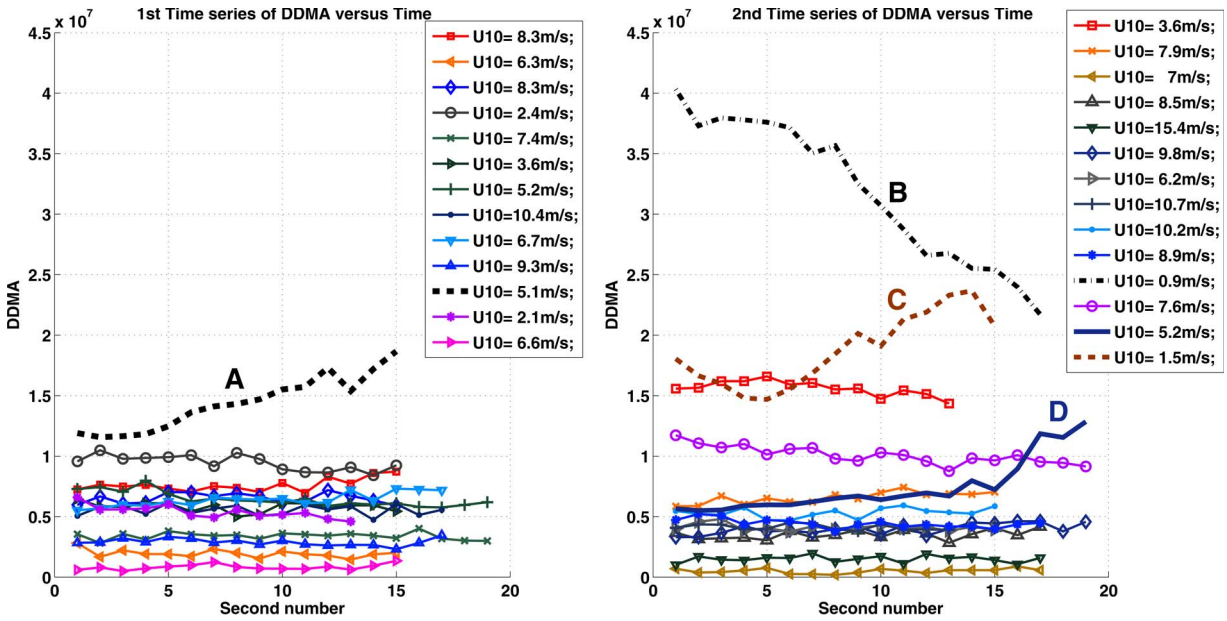


Fig. 4. Plot of 50-ms DDMA versus time, for all of the 27 UK-DMC overpasses collocated with NDBC buoys.

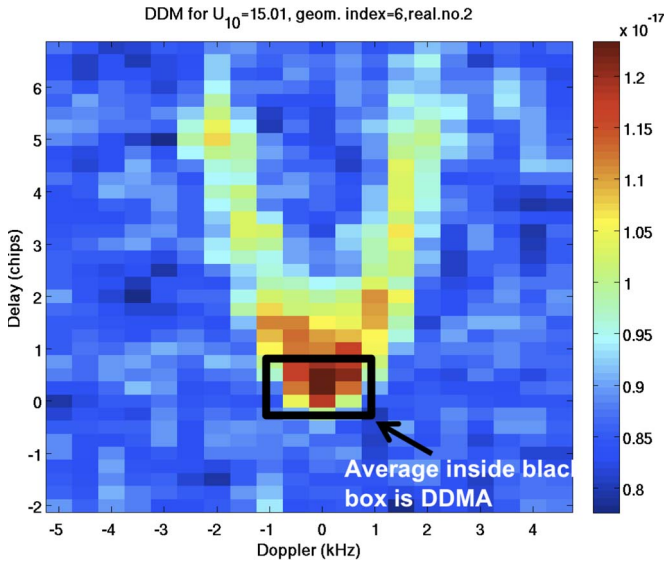


Fig. 5. Illustration of a DDM and of the area where the DDMA is calculated.

The open-loop tracking algorithm used to compute the DDM aligns the zero-delay and zero-Doppler to its best estimate of the SP position. The resultant DDM can have an actual SP position offset due to differences in path length between the modeled earth geoid and the true ocean surface, as well as other delays such as are due to atmospheric refractivity. Here, we compute the SP location in the DDM as the position of Most Probable Maximum. The location is estimated as the position with the highest number of occurrences of the maximum power value, across the total number of 1-second DDMs for each data stream.

The choice of the delay and Doppler ranges is a tradeoff between the improvement in signal-to-noise that results from averaging across more of the diffuse scattered signal in the glistening zone, versus the improvement in spatial resolution that results from only averaging over a limited region. A more detailed examination of the correspondence between spatial resolution and the delay and Doppler ranges selected for all of the observables is provided in Section IV-F.

The DDMA is calculated from DDMs after an estimate of its noise floor has been subtracted. The noise floor is estimated directly from each DDM by averaging over a region where there is no scattered signal (specifically, at delay values between -6 chips and -3.4 chips before the SP), and is then subtracted from each DDM pixel. For UK-DMC DDMs, we estimate the noise floor as the average over the full Doppler range (i.e., 10 kHz) and over the first 3 chips (i.e., the first 16 rows of the DDM). This region has been verified to contain only noise in all the UK-DMC overpasses under examination. A single value for the noise floor is computed for each overpass using all of the 1-second DDMs.

From these DDMs, the DDMA is calculated as the average scattered power over a delay range of 0.75 chips and a Doppler range of 2 kHz. The Doppler range is symmetrically chosen about the SP, while the delay range is chosen from -0.2 chips, to $+0.55$ chips, where 0 chips is referenced as the delay of the SP. The delay range begins one delay sample before the SP, rather than at the SP itself, since the samples adjacent to the SP still contain a good amount of the scattered power from the SP pixel, due to the power spreading caused by the Woodward Ambiguity Function (WAF). The DDMA is computed for each 1-second DDM, resulting in a stream of between 13 and 19 DDMA values for each UK-DMC overpass.

In order to generate an empirical GMF relating the DDMA to ocean surface wind speed, the individual 1-second DDMs are averaged together for each of the overpasses. This reduces the noise present in the training data used for the GMF and it normalizes the number of samples present at each wind speed. Averaging in this way does not significantly smooth the response of the DDMA to wind speed because of the filtering that was applied to remove the cases of non-uniform winds. The resulting scatterplot of DDMA and collocated NDBC buoy

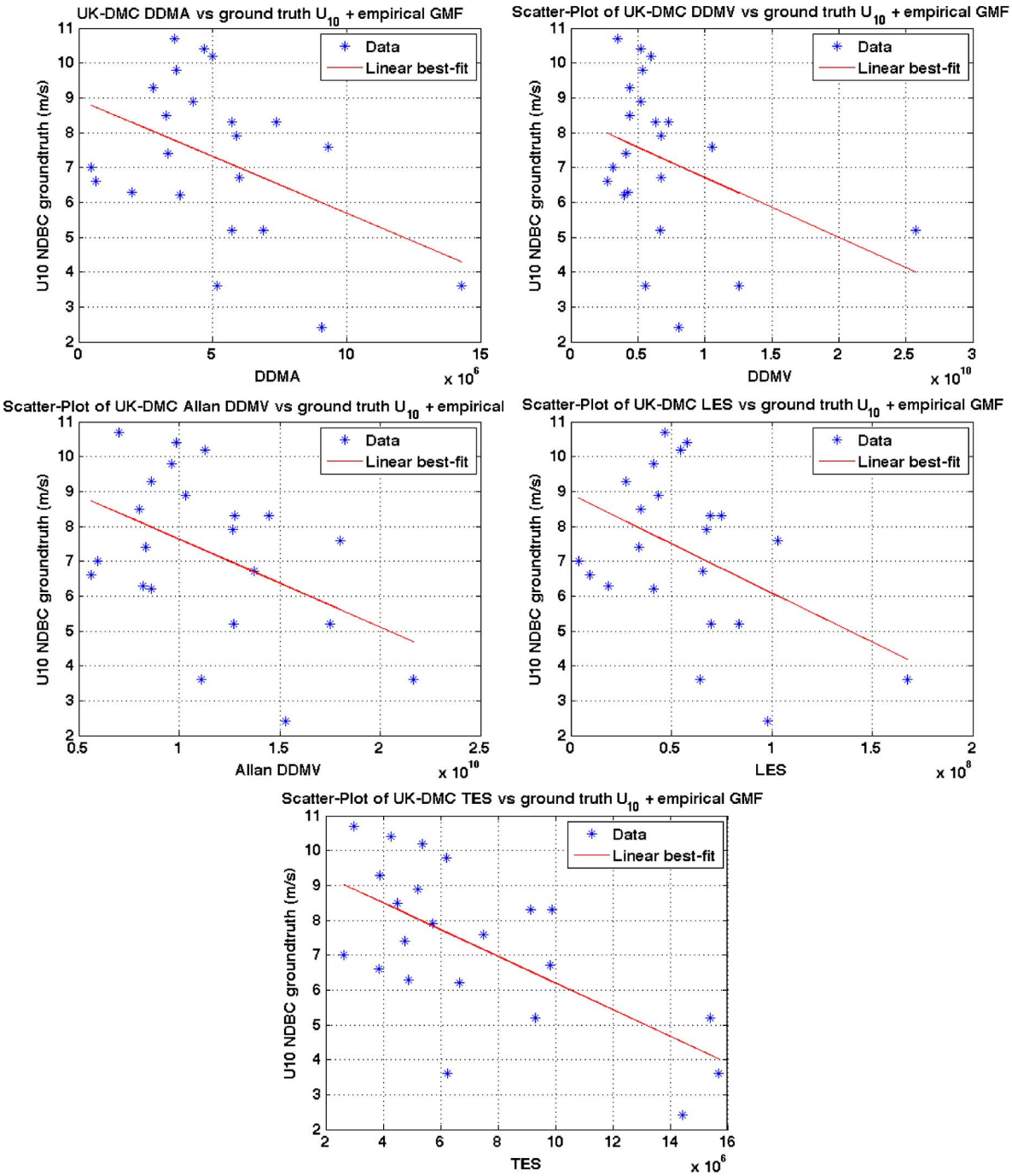


Fig. 6. Scatterplot of (top left) DDMA, (top right) DDMV, (center left) ADDMV, (center right) LES, and (bottom center) TES observables, versus collocated wind speed, along with the best-fit linear empirical GMF.

wind training data for the GMF is shown in Fig. 6 (top left). The red line is the empirical GMF, derived as a least squares first order polynomial fit to the data. In this case, and for the other observables as well, we opt for a simple linear function as the GMF, since higher order polynomial fits and other types of functional forms did not provide a significantly better fit. The correlation coefficient (r) and explained variance (R^2) of the linear fit are -0.44 and 0.19, respectively. The fairly low value of explained variance is in part due to the need to filter the dynamic range of wind speeds considered (due to the AGC issue), which limits the total variance of the winds. This, in turn, causes the unexplained variance in the scatter plots (due to retrieval errors and other noise effects) to be a higher fraction of the total than would be expected given a wider dynamic range of wind speeds. We anticipate that these results will improve when the restriction on the dynamic range of winds can be lifted with future GNSS-R missions.

The winds from each 1-second DDMA sample are then estimated using the empirical GMF. The performance of the retrieval is measured as the Root-Mean Square (RMS)

TABLE II
RMS WIND SPEED RETRIEVAL ERROR FOR EACH OF FIVE DDM OBSERVABLES AND FOR THE COMPOSITE MV ESTIMATOR

	RMS Error (m/s)
DDMA	2.01
DDMV	2.08
ADDMV	1.99
LES	2.00
TES	1.70
MV	1.65

difference between the estimated winds and the NDBC ground truth winds, or

$$\mathrm{RMS_{ERR}} = \sqrt{\frac{1}{L}\sum_{l=1}^{L}\left(U^{l}_{10(est)} - U^{l}_{10(\mathrm{true})}\right)^2}. \tag{4.2}$$

The RMS error in the DDMA retrieval is found in this way to be 2.01 m/s (see Table II).

B. Delay-Doppler Map Variance (DDMV)

The Delay-Doppler Map Variance is defined as the variance of the population of DDMAs measured during a buoy overpass. The incoherent averaging time of the DDMs from which the DDMA are computed is reduced from 1 second to 50 ms in order to enhance the sensitivity of the observable to the wind speed.

The DDMV exploits the speckle noise that is present in the DDM, in particular its dependence on the surface roughness and wind. Speckle is here no longer considered as noise, but as an additional source of information about the wind speed. For flat surfaces, or surfaces characterized by very low wind, the glistening zone in the DDM of scattered power reduces to a concentrated peak near the SP and with reduced speckle. For a wind roughened surface, the sea surface facets are tilted and oriented in different directions, generating more scattered power away from the SP, and also more speckle from the random fluctuations caused by constructive/destructive interference of the signal scattered from different facets. These fluctuations, which generate the speckle noise, grow stronger with increasing winds. As a consequence, the intensity of speckle noise, as characterized by the variance, is related to the wind speed. Speckle noise is a short time scale process that is accentuated by performing shorter, 50 ms, incoherent averaging of the DDMs. It should be noted that the variance of the DDMA scales with its magnitude, so that the dependence of the DDMV observable on wind speed will include a component that is correlated with the DDMA observable as well as a component due to the speckle itself.

The DDMV is computed as the variance of the DDMA values calculated from the population of 50 ms DDMs for each overpass, or

$$\mathrm{DDMV}(\Delta\tau,\Delta f) = \frac{1}{I}\sum_{i=1}^{I}\left\{\mathrm{DDMA}_Y(\Delta\tau,\Delta f,t_i) - \langle \mathrm{DDMA}_Y(\Delta\tau,\Delta f)\rangle\right\}^2 \tag{4.3}$$

where the individual time samples, t_i, are now every 50 ms and the $< >$ operator is the average over the full population. The individual UK-DMC overpasses last between 13 and 19 seconds, resulting in $260 < \mathrm{I} < 380$ DDMs in each population.

The DDMV is computed using the same delay and Doppler ranges, $\Delta\tau$ and Δf, as was the DDMA in Section IV-A, hence the spatial resolution is the same. A scatterplot of the DDMV observable versus NDBC buoy wind speed is shown in Fig. 6 (top right), together with the best-fit linear GMF. The best-fit figures of merit are $r = -0.36$ and $\mathrm{R}^2 = 0.13$. In the scatterplot, the overall trend is for the DDMV to decrease with increasing wind speed, which suggests that the scaling of the DDMV by the magnitude of the DDMA is the dominant source of explained variance, whereas the increase in speckle with wind speed is only a secondary explanation. This is corroborated by the fairly high correlation between the errors in the two wind retrievals based on these observables (see Section V). The RMS error in the DDMV retrieval is 2.08 m/s (see Table II).

C. Allan Delay-Doppler Map Variance

The Allan DDM Variance (ADDMV) is defined as the variance of the population of differences between consecutive DDMAs measured during a selected interval of time. The ADDMV used here as a DDM observable is computed using an incoherent integration time of 50 ms, similarly to the DDMV observable, or

$$\mathrm{ADDMV}(\Delta\tau,\Delta f) = \frac{1}{I-1} \times \sum_{i=2}^{I}\left\{\overline{\mathrm{DDMA}_Y(\Delta\tau,\Delta f,t_i)} - \overline{\mathrm{DDMA}_Y(\Delta\tau,\Delta f,t_{i-1})}\right\}^2 \tag{4.4a}$$

where

$$\overline{\mathrm{DDMA}_Y(\Delta\tau,\Delta f,t_i)} = \mathrm{DDMA}_Y(\Delta\tau,\Delta f,t_i) - \langle \mathrm{DDMA}_Y(\Delta\tau,\Delta f)\rangle\,. \tag{4.4b}$$

The Allan variance is used to characterize the short time scale variability of random processes by cancelling out longer term variations that are common to consecutive samples [49]. In our case, the objective is the removal of slowly varying changes such as might be due to receiver gain drifts or wind speed non-uniformity in order to better isolate the speckle component of the variations. The ADDMV is computed using the same delay and Doppler ranges, $\Delta\tau$ and Δf, as the DDMA and DDMV, so it also has the same spatial resolution. A scatterplot of the ADDMV observable versus the NDBC buoy wind speed is shown in Fig. 6 (center left), together with the best-fit linear GMF. The best-fit figures of merit are $r = -0.45$ and $\mathrm{R}^2 = 0.21$. The RMS error in the ADDMV retrieval is 1.99 m/s (see Table II).

D. Leading Edge Slope (LES) of Integrated Delay Waveforms

The Leading Edge Slope (LES) is defined as the slope of the leading edge of the Integrated Delay Waveform (IDW). The

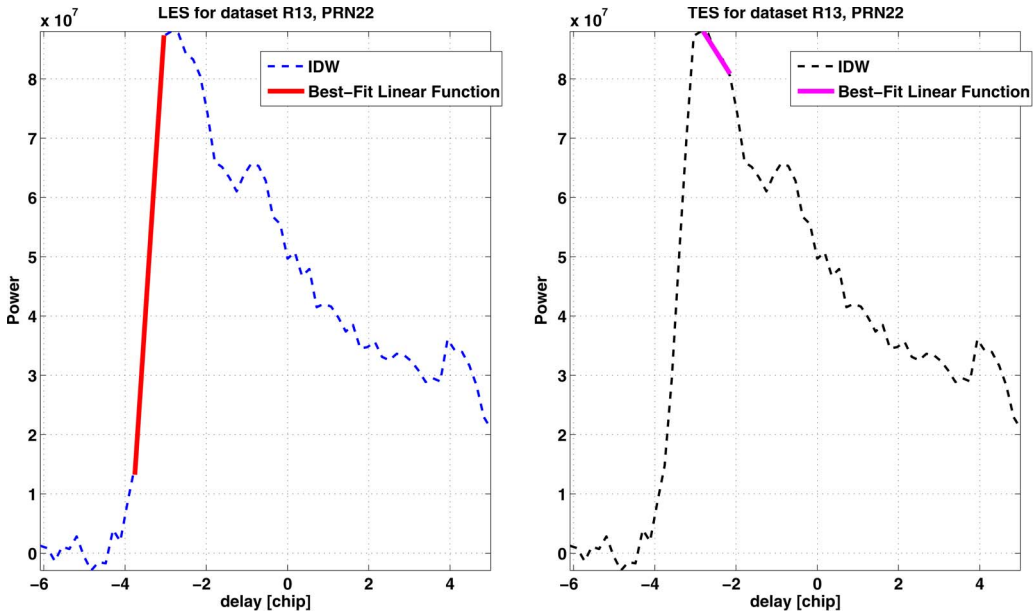


Fig. 7. Illustration of best-fit linear function for the (left) leading edge and the (right) trailing edge of an IDW.

IDW is obtained by incoherently integrating the DDM over a specified range of Doppler frequencies, giving the scattered power as a function of delay only. The IDW resembles the backscattered waveform used in conventional radar altimetry [50], which are also characterized by a leading edge with a slope from which the Significant Wave Height (SWH) of the ocean surface can be estimated. The LES can be written as

$$\alpha(\Delta\tau,\Delta f,t_i)=\underset{\alpha,c}{\arg\min}\left\{\left[\sum_{k=1}^{2}I(\tau_k,\Delta f,t_i)-(\alpha\tau_k+c)\right]^2\right\}$$

$$I(\tau_k,\Delta f,t_i)=\frac{1}{N}\sum_{n=1}^{N}\overline{Y}(\tau_k,f_n,t_i) \tag{4.5}$$

where $\Delta\tau=\tau_2-\tau_1$ is the delay interval over which the LES α is calculated. An example of the IDW and the best-fit linear function along its leading edge is illustrated in Fig. 7 (left). The LES is calculated using IDWs obtained from 1-second incoherent integration DDMs. The Doppler range is kept the same for all the observables, to maintain consistency in spatial resolution among the wind estimates from the different observables. The delay range of the IDW over which the slope is computed is also kept equal to that used for the other observables, and centered at the central point of the leading edge of the waveform.

The portion of the leading edge of the IDW where the slope is calculated is centered around the point of maximum slope in the leading edge, i.e., the point with maximum derivative. However, there is in some cases some ambiguity in identification of such point, especially when the waveforms are particularly noisy. We then compute the coefficients of the first order polynomial function that best fits the IDW, over the portion of the leading edge chosen to calculate the LES, and select the slope of this function (i.e., the first of the two coefficients obtained from the fit) as our LES observable. A scatterplot of the LES versus NDBC buoy wind speed is shown in Fig. 6, (center right), together with the best-fit linear GMF. The best-fit figures of merit are $r=-0.44$ and $\mathrm{R}^2=0.20$. The RMS error in the LES retrieval is 2.00 m/s (see Table II).

E. Trailing Edge Slope (TES) of Integrated Delay Waveforms

The IWV also has a trailing edge whose slope responds to changes in the wind speed. The Trailing Edge Slope (TES) is calculated as the slope of the waveform region extending from the waveform peak to 0.75 chips from the peak, where the position of the peak in the waveform is computed as the delay value with the most probable maximum in the DDM. Similarly as the LES, the TES is computed as the slope of the best-fit line to the waveform in the region specified. An example of the best-fit linear function at the trailing edge of the IDW is shown in Fig. 7 (right). Mathematically, the TES can be expressed as

$$\beta(\Delta\tau,\Delta f,t_i)=\underset{\beta,\boldsymbol{d}}{\arg\min}\left\{\left[\sum_{k=3}^{4}J(\tau_k,\Delta f,t_i)-(\beta\tau_k+d)\right]^2\right\}$$

$$J(\tau_k,\Delta f,t_i)=\frac{1}{N}\sum_{n=1}^{N}\overline{Y}(\tau_k,f_n,t_i) \tag{4.6}$$

where $\delta\tau_{\mathrm{TES}}=\tau_4-\tau_3$ is the delay interval over which the TES slope is calculated. As with the LES, the TES is estimated for each 1-second DDM of each overpass. A scatterplot of the TES observable versus NDBC buoy wind speed is shown in Fig. 6 (bottom, center), together with the best-fit linear GMF. The best-fit figures of merit are $r=-0.65$ and $\mathrm{R}^2=0.42$. The RMS error in the TES retrieval is 1.70 m/s (see Table II).

F. Spatial Resolution

The spatial resolution of each observable depends on both the delay-Doppler range used to calculate the observables, and on the WAF, which spreads the power coming from a given delay-Doppler pixel (i.e., a given spatial area) to adjacent pixels. For

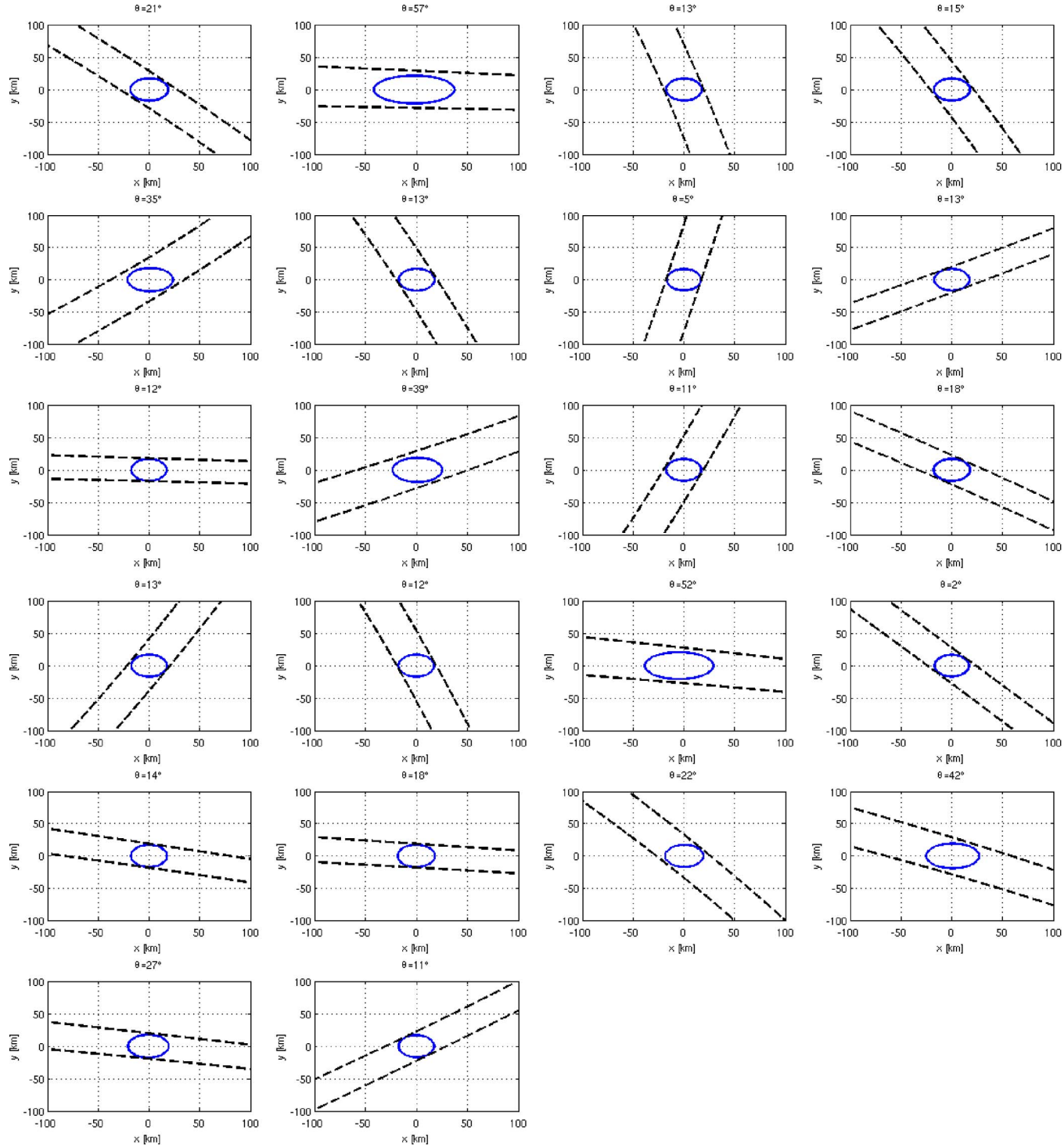


Fig. 8. Iso-delay lines at 0.75 chips and iso-Doppler lines at 2 kHz for all of the geometries encountered during the UK-DMC overpasses. In each case, the geometry illustrated is for the first second of the data stream.

regions of the DDM that do not include the SP, there is also an ambiguity due to the fact that each pixel contains contributions from two different regions in space as a result of the double intersection of an iso-Doppler line with an iso-delay line [37]. However, the observables considered here are not affected by this ambiguity. The delay-Doppler region over which our observables is calculated (0.75 chips and 2 kHz) is large enough that the WAF spreading is a second order correction to the spatial resolution. For that reason, it is neglected here. Fig. 8 shows plots of the iso-delay contours at 0.75 chips and the iso-Doppler contours at 2 kHz over a 200×200 km^2 area, for the 22 overpasses considered. The choice of delay and Doppler ranges are seen to be consistent with one another, since the iso-Doppler lines tend to intersect the edges of the iso-delay ellipses. This guarantees that all available scattered power within the iso-delay ellipse will be included in the processed region of

the DDM. Decreasing the Doppler range would remove some of the scattered power and increasing it further would only add more noise, but not scattered signal, to the processed region. Each plot specifies the incidence angle in its title, which is the angle between the forward scattered signal and the local normal to the surface. The iso-delay ellipses tend to increase in size at higher incidence angles, which degrades (i.e., enlarges) the spatial resolution.

If the Doppler range is properly set, the major and minor axes of the iso-delay ellipse determine the spatial resolution. With a 0.75 chip delay range, the major axis ranges between 34 km and 84 km, while the minor axis ranges between 34 km and 44 km. These dimensions set the instantaneous scattering area of the observables. An effective spatial resolution must additionally include the smearing of the instantaneous ellipse due to spacecraft orbital motion. In the case of UK-DMC, this amounts to approximately 6 km/s of beam smearing by the instantaneous ellipse in the ground track direction.

V. Minimum Variance Estimator

The five individual estimates of the wind speed can be combined together to produce a Minimum Variance (MV) estimator. A MV estimator exploits the degree of decorrelation between the errors in the individual estimates to minimize the RMS error in its wind speed estimate [51]. The advantage of such an estimator lies in the fact that its RMS error will always be better than or equal to the lowest RMS error in the retrieved wind speeds among the individual observables. The lower the correlation between errors in pairs of individual estimators, the better the RMS error performance of the MV estimator. The MV estimator is built as a linear combination of the original estimators, according to

$$u_{\mathrm{MV}} = \boldsymbol{m} \cdot \boldsymbol{u} \tag{4.7}$$

where $\vec{u}$ is the vector of individual estimates and $\vec{m}$ is the vector of coefficients. The coefficients are obtained by requiring that the MV estimator be unbiased (i.e., the expected value of its retrieval is equal to the true quantity to be estimated) and by minimizing its variance. The estimator is derived in the Appendix. The coefficients of the linear combination are given by

$$\boldsymbol{m} = \left(\sum_{i=1}^{N} \sum_{j=1}^{N} c_{i.j}^{-1} \right)^{-1} \boldsymbol{C}^{-1} \mathbf{1} \tag{4.8}$$

where $\mathbf{1}$ is a vector of ones, $\boldsymbol{C}^{-1}$ is the inverse of the covariance matrix between the individual retrieval errors, and $c_{i.j}^{-1}$ are its elements. The variance of the MV estimator is given by

$$\sigma_{\mathrm{MV}}^2 = \left(\sum_{i=1}^{N} \sum_{j=1}^{N} c_{i.j}^{-1} \right)^{-1}. \tag{4.9}$$

The MV estimator requires knowledge of the covariance matrix of the individual retrieval errors. The covariance is estimated empirically from the errors in overpass retrievals.

TABLE III
Correlation Between the Retrieval Errors by Each Pair of Observables

	DDMA	DDMV	ADDMV	LES	TES
DDMA	1.00	0.91	0.98	0.99	0.90
DDMV		1.00	0.94	0.91	0.88
ADDMV			1.00	0.98	0.92
LES				1.00	0.90
TES					1.00

The covariance matrix can be factored into two component matrices, as

$$\boldsymbol{C} = \boldsymbol{SRS} \tag{4.10}$$

where $\boldsymbol{S}$ is a diagonal matrix of standard deviations of the retrieval errors for each observable (i.e., the square root of the diagonal elements of the covariance matrix), and $\boldsymbol{R}$ is the matrix of correlation coefficients, whose elements are always between -1 and 1. The five standard deviations and the correlation matrix are listed in Tables II and III. A visual illustration of this correlation is provided in Fig. 9, where scatter plots of retrieval errors by pairs of observables are shown for the pairs of observables with the highest (0.99) and lowest (0.88) correlation coefficients. The highest correlation exists between DDMA and LES retrievals, while the lowest correlation exists between DDMV and TES retrievals. In general, retrieval errors by the TES observable have the lowest correlation with those by the other observables.

Fig. 10 shows a scatter plot of the wind speed retrieved by the MV estimator versus the ground truth buoy wind speed. The RMS error in the MV estimator was evaluated directly as the RMS difference between retrieved and ground truth winds, using eq. (4.2), and analytically using eq. (4.9). In both cases, the error is equal to 1.65 m/s. The MV retrieval error is lower than that of each of the 5 individual observables. Table II summarizes the RMS errors in the retrievals using each of the five individual observables as well as the RMS error using the composite MV estimator.

The same 22 data samples are used for both the training data from which the GMFs are derived for the five observables, as well as for the RMS error performance assessment. It would be preferable to use independent data sets, but our approach was driven by the limited number of data samples available from the UK-DMC mission. As a means of demonstrating that the reported retrieval performance is not a result of artificial tuning of the retrieval to the particular data samples, we repeated the retrieval analysis after splitting the data into 11 training samples and 11 samples used for performance assessment. After doing so, the RMS wind speed retrieval error for the minimum variance estimator changes slightly, from 1.65 m/s when all 22 samples are used for both training and performance assessment, to either 1.45 or 1.70 m/s when the samples are split into two independent subsets. The two RMS error values depend on which subset is used to train and which to assess. The changes are likely due to the standard error in the estimate of the RMS retrieval error, and are associated with the small population size.

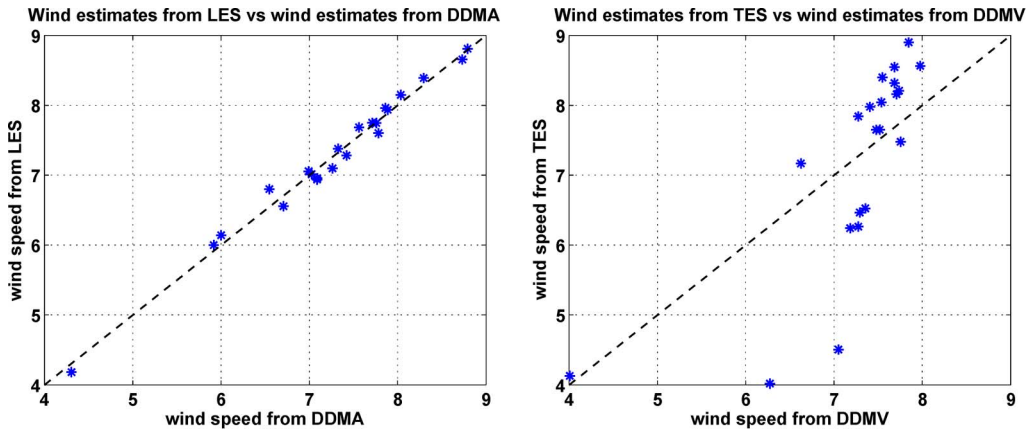


Fig. 9. Scatterplots of wind speed retrieved using two different DDM observables. (Left) The highest correlation in the retrieval errors (99%) is between the DDMA and LES retrievals. (Right) The lowest correlation (88%) is between the DDMV and TES retrievals.

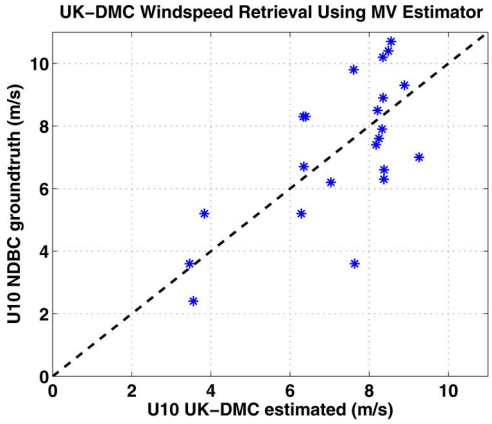


Fig. 10. MV wind speed estimate versus NDBC buoy ground-truth winds. The RMS difference between them is 1.65 m/s.

VI. Discussion

The DDMs from which all 5 observables were derived are calibrated in units proportional to the received power at the UK-DMC satellite. With conventional backscatter radars, it is common to develop remote sensing retrieval algorithms that depend on the normalized radar cross section (NRCS) of the surface. The NRCS is derived from the received power by correcting for its dependence on transmit power, transmit and receive antenna gain, scattering area, and propagation path loss. This is done in order to isolate and emphasize the component of variance in the received power that is explained by variations in the surface conditions.

In our case, the presence of an Automatic Gain Control (AGC) circuit in the UK-DMC receiver precluded the advantages of a conversion from received power to NRCS. The AGC circuit made corrections to the receiver gain in order to keep the signal being digitized within the limited analog to digital converter range. The UK-DMC data samples with the highest and lowest wind speed ground truth values were removed from our consideration in order to limit the dynamic range of the scattered signal. In this way, the scattered power becomes only a relatively small component of the total signal and the AGC response is dominated by changes in the system noise power (receiver noise + Earth brightness temperature + interference). The detrimental impact of AGC on the dynamic range of observable winds, and the uncertainty it introduces into the measurement of absolute scattered power (as opposed to relative signal-to-noise ratio), have motivated the option to disable AGC and replace it with manual, ground controlled, gain adjustments in the upcoming GNSS-R missions: TechDemoSat-1 and CYGNSS.

One other distinction should be noted between the UK-DMC measurements and those expected by TechDemoSat-1 and CYGNSS. UK-DMC telemetered raw sampled IF data to the ground, which allows for DDMs to be generated with any temporal sampling. In particular, 1-second samples were used for the DDMA, LES and TES observables and 50-millisecond samples were used for the DDMV and ADDMV observables. While both TechDemoSat-1 and CYGNSS will have a similar "raw IF" data mode, and will thus be capable of generating the same set of 5 observables, that mode can only be operated on orbit with a limited duty cycle due to the large data rates involved. In the case of CYGNSS, nominal, full-time operation (i.e., 100% duty cycle) will only be possible if the DDMs are generated on board with 1-second temporal resolution and are then telemetered to the ground. This "DDM" data mode will only support generation of the DDMA, LES and TES observables. Application of the MV estimator to this reduced set of three observables results in an RMS error retrieval performance of 1.68 m/s, which is only slightly degraded relative to the full 5-observable version.

The correlation between retrieval errors using the individual observables is in general quite high. This is partly to be expected because they are all derived from the same DDM and from the same region of it near the SP. In the case of the DDMA observable, additional correlation is to be expected with both the DDMV and ADDMV since the latter two observables are sensitive to the speckle noise present in the scattered signal and speckle is known, on average, to be proportional to the scattered power. However, their correlations are below 100% because the proportionality is only true on average, but not for noisy individual estimates of the power and variance statistics. Both the DDMA estimate of scattered power and the variance-based observable estimates related to speckle are derived from finite sample populations and, hence, are noisy. The observed

decorrelation values indicate that the standard errors in their estimates are not completely correlated, so including all of them in the minimum variance estimator helps to reduce the aggregate error. Some of the correlation is also due to the way the data samples used in this study were selected and processed. Pre-filtering was applied to the overpass data set to remove cases with highly non-uniform wind fields, in order to improve their correspondence with the collocated NDBC buoy measurements. This likely contributed to the high correlation that existed between DDMV and ADDMV retrievals. Both of these observables are measures of the variability in the signal, with the DDMV responding to variability on all time scales and the ADDMV responding only to short time scale processes. Their high correlation suggests that the short time scale processes are dominant, which is to be expected given the pre-filtering that was applied. When this wind speed retrieval algorithm is applied later to a wider variety of non-uniform data, it can be expected that the correlation between DDMV and ADDMV retrieval errors will decrease and their unique contributions to the MV estimator will improve.

VII. Conclusion

A Minimum Variance (MV) wind speed estimator is constructed from five observables derived from GNSS-R Delay Doppler Maps (DDMs). The observables exploit properties of the DDM that respond to variations in the ocean surface wind speed. The observables include the Delay-Doppler Map Average (DDMA), the Delay-Doppler Map Variance (DDMV), Allan Delay-Doppler Map Variance (ADDMV), Leading Edge Slope (LES), and Trailing Edge Slope (TES). Each of these observable is introduced here for the first time as a means of extracting wind speed information from the DDMs. The observables are calculated, and the wind speed retrieval algorithms tested, using spaceborne GPS-R DDMs, collected during the UK-DMC mission. Ground-truth winds are provided by NDBC buoys that are collocated with the UK-DMC measurements. A simple wind retrieval algorithm is developed individually for each observable using an empirical GMF that is derived by linear regression of the observable against the ground-truth wind speed. The MV estimator is constructed as a linear combination of the wind estimates from each observable. It shows improved performance, in terms of RMS difference between estimated and ground-truth wind, compared to the retrieval by each individual observable. The improvement is not large because the correlation between observables is high. However, what partial decorrelation does exist is fully exploited by the MV estimator to lower the overall RMS error, which is 1.65 m/s when all the five observables are used, and 1.68 m/s when only the observables derived from 1-second DDMs are used.

Appendix
Derivation of Minimum Variance (MV) Estimator

Notation:

—Scalar quantities are designated by lower case variables, e.g., 1.

—Vector quantities are designated by variables with a vector arrow above them, e.g., $\vec{m}$.

—Estimated quantities are designated by variables with a "hat" above them, e.g., $\hat{u}$.

—Matrices are designated by upper case, boldfaced variables, e.g., $\boldsymbol{C}$.

The Minimum Variance (MV) estimator, $\hat{u}_{\mathrm{MV}}$, is constructed as a linear combination of individual wind speed estimates, or

$$\hat{u}_{\mathrm{MV}} = \vec{m} \cdot \hat{u} \tag{A1}$$

where $\vec{m}$ is a vector of linear combination coefficients and $\hat{u}$ a vector of the individual wind speed estimates. In our case, they are derived from the five DDM observables: DDMA, DDMV, Allan DDMV, LES and TES. The coefficients in the MV estimator are properly normalized by the following constraint:

$$\vec{m} \cdot \vec{1} = 1 \tag{A2}$$

where $\vec{1}$ is a vector of all ones.

Let $\boldsymbol{C}$ be the covariance matrix for errors in the individual wind speed estimates, or

$$C_{ij} = \langle (u_i - u_{\mathrm{true}})(u_j - u_{\mathrm{true}}) \rangle \tag{A3}$$

where u_i is the wind speed estimated from the ith DDM observable and u_{true} is the true wind speed. The variance of the MV estimator is given by

$$\sigma^2_{\mathrm{MV}} = \left\langle (u_{\mathrm{MV}} - u_{\mathrm{true}})^2 \right\rangle. \tag{A4}$$

Substituting (A1) into (A4), expanding the square, and using the expression (A3) for the elements of the covariance matrix, (A4) can be rewritten as

$$\sigma^2_{\mathrm{MV}} = \vec{m} \cdot \boldsymbol{C} \cdot \vec{m}'. \tag{A5}$$

Minimization of σ^2_{MV} with respect to the elements of $\vec{m}$, subject to the constraint given by (A2), is performed using the Method of Lagrange Multipliers, or

$$\nabla \left(\sigma^2_{\mathrm{MV}} + \lambda \vec{m} \cdot \vec{1} \right) = 2\boldsymbol{C} \cdot \vec{m}' + \lambda \cdot \vec{1} = 0 \tag{A6}$$

where λ is the Lagrange multiplier. Solving for $\vec{m}$ in (A6) gives

$$\vec{m} = -\frac{\lambda}{2} \boldsymbol{C}^{-1} \cdot \vec{1}. \tag{A7}$$

Substitution of (A7) into (A2) solves for the Lagrange multiplier as

$$\lambda = -2 \left(\sum_{i=1}^{N} \sum_{j=1}^{N} C^{-1}_{ij} \right)^{-1} \tag{A8}$$

where C^{-1}_{ij} is the ijth elements of the inverse of the covariance matrix $\boldsymbol{C}^{-1}$, and N is the dimensionality of $\vec{m}$. The final form

of the solution for the minimum variance coefficients is found by inserting (A8) into (A7), giving

$$\vec{m} = \left(\sum_{i=1}^{N} \sum_{j=1}^{N} C_{ij}^{-1} \right)^{-1} \boldsymbol{C}^{-1} \cdot \vec{1}. \tag{A9}$$

Substituting (A9) in (A5) gives an expression for the variance of the MV estimator as

$$\sigma_{\mathrm{MV}}^2 = \left(\sum_{i=1}^{N} \sum_{j=1}^{N} C_{ij}^{-1} \right)^{-1}. \tag{A10}$$

Note that the derivation presented here is valid for an arbitrary number, N, of individual estimators.

REFERENCES

[1] A. Stoffelen and D. L. T. Anderson, "Wind retrieval and ERS-1 scatterometer radar backscatter measurements," *Adv. Space Res.*, vol. 13, no. 5, pp. 53–60, May 1993.

[2] D. W. Draper and D. G. Long, "An assessment of SeaWinds on QuikSCAT wind retrieval," *J. Geophys. Res.*, vol. 107, no. C12, pp. 5-1–5-14, Dec. 2002.

[3] J. Figa-Saldaña, J. J. W. Wilson, E. Attema, R. Gelsthorpe, M. R. Drinkwater, and A. Stoffelen, "The Advanced Scatterometer (ASCAT) on the Meteorological Operational (MetOp) platform: A follow on for the European wind scatterometers," *Can. J. Remote Sens.*, vol. 28, no. 3, pp. 404–412, Jun. 2002.

[4] D. B. Chelton, M. H. Freilich, J. M. Sienkiewicz, and J. M. Von Ahn, "On the use of QuikSCAT scatterometer measurements of surface winds for marine weather prediction," *Mon. Wea. Rev.*, vol. 134, no. 8, pp. 2055–2071, Aug. 2006.

[5] M. Portabella and A. Stoffelen, "Scatterometer backscatter uncertainty due to wind variability," *IEEE Trans. Geosci. Remote Sens.*, vol. 44, no. 11, pp. 3356–3362, Nov. 2006.

[6] B. S. Gohil, A. Sarkar, A. K. Varma, and V. K. Agarwal, "Wind vector retrieval algorithm for Oceansat-2 scatterometer," in *Proc. SPIE, Microw. Remote Sens. Atmos. Environ. V*, 2006, vol. 6410, p. 64100S.

[7] J. Verspeek, A. Stoffelen, A. Verhoef, and M. Portabella, "Improved ASCAT wind retrieval using NWP ocean calibration," *IEEE Trans. Geosci. Remote Sens.*, vol. 50, no. 7, pp. 2488–2494, Jul. 2012.

[8] D. B. Chelton and P. J. McCabe, "A review of satellite altimeter measurement of sea surface wind speed: With a proposed new algorithm," *J. Geophys. Res.*, vol. 90, no. C3, pp. 4707–4720, May 1985.

[9] G. Chen, B. Chapron, R. Ezraty, and D. Vandemark, "A dual-frequency approach for retrieving sea surface wind speed from TOPEX altimetry," *J. Geophys. Res., Oceans*, vol. 107, no. C12, pp. 19-1–19-10, Dec. 2002.

[10] C. P. Gommenginger, M. A. Srokosz, P. G. Challenor, and P. D. Cotton, "Development and validation of altimeter wind speed algorithms using an extended collocated Buoy/Topex dataset," *IEEE Trans. Geosci. Remote Sens.*, vol. 40, no. 2, pp. 251–260, Feb. 2002.

[11] C. C. Wackerman, C. Rufenach, R. A. Shuchman, J. A. Johannessen, and K. L. Davidson, "Wind vector retrieval using ERS-1 synthetic aperture radar imagery," *IEEE Trans. Geosci. Remote Sens.*, vol. 34, no. 6, pp. 1343–1352, Nov. 1996.

[12] J. Horstmann, H. Schiller, J. Schulz-Stellenfleth, and S. Lehner, "Global wind speed retrieval from SAR," *IEEE Trans. Geosci. Remote Sens.*, vol. 41, no. 10, pp. 2277–2286, Oct. 2003.

[13] F. M. Monaldo, D. R. Thompson, R. C. Beal, W. G. Pichel, and P. Clemente-Colon, "Comparison of SAR-derived wind speed with model predictions and ocean buoy measurements," *IEEE Trans. Geosci. Remote Sens.*, vol. 39, no. 12, pp. 2587–2600, Dec. 2001.

[14] H. Hersbach, A. Stoffelen, and S. de Haan, "An improved C-band scatterometer ocean geophysical model function: CMOD5," *J. Geophys. Res.*, vol. 112, no. C3, pp. C03006-1–C03006-18, Mar. 2007.

[15] J. A. Verspeek, A. Stoffelen, M. Portabella, H. Bonekamp, C. Anderson, and J. Figa, "Validation and calibration of ASCAT using CMOD5.n," *IEEE Trans. Geosci. Remote Sens.*, vol. 48, no. 1, pp. 386–395, Jan. 2010.

[16] S. Soisuvarn, Z. Jelenak, P. S. Chang, S. O. Alsweiss, and Q. Zhu, "CMOD5.H—A high wind geophysical model function for C-band vertically polarized satellite scatterometer measurements," *IEEE Trans. Geosci. Remote Sens.*, vol. 51, no. 6, pp. 3744–3760, Jun. 2013.

[17] B. S. Gohil, R. Sikhakolli, and R. K. Gangwar, "Development of geophysical model functions for Oceansat-2 scatterometer," *IEEE Geosci. Remote Sens. Lett.*, vol. 10, no. 2, pp. 377–380, Mar. 2013.

[18] S. T. Brown, C. S. Ruf, and D. R. Lyzenga, "An emissivity-based wind vector retrieval algorithm for the WindSat polarimetric radiometer," *IEEE Trans. Geosci. Remote Sens.*, vol. 44, no. 3, pp. 611–621, Mar. 2006.

[19] F. J. Wentz, "A well-calibrated ocean algorithm for special sensor microwave/imager," *J. Geophys. Res.*, vol. 102, no. C4, pp. 8703–8718, Apr. 1997.

[20] M. Martin-Neira, M. Caparrini, J. Font-Rossello, S. Lannelongue, and C. S. Vallmitjana, "The PARIS concept: An experimental demonstration of sea surface altimetry using GPS reflected signals," *IEEE Trans. Geosci. Remote Sens.*, vol. 39, no. 1, pp. 142–150, Jan. 2001.

[21] J. Garrison, S. Katzberg, and M. Hill, "Effect of sea roughness on bistatically scattered range coded signals from the global positioning system," *Geophys. Res. Lett.*, vol. 25, no. 13, pp. 2257–2260, Jul. 1998.

[22] V. Zavorotny and A. Voronovich, "Scattering of GPS signals from the ocean with wind remote sensing applications," *IEEE Trans. Geosci. Remote Sens.*, vol. 38, no. 2, pp. 951–964, Mar. 2000.

[23] J. Garrison, A. Komjathy, V. Zavorotny, and S. J. Katzberg, "Wind speed measurements using forward scattered GPS signals," *IEEE Trans. Geosci. Remote Sens.*, vol. 40, no. 1, pp. 50–65, Jan. 2002.

[24] S. T. Lowe, J. L. LaBrecque, C. Zuffada, L. Romans, L. Young, and G. Hajj, "First spaceborne observation of an earth-reflected GPS signal," *Radio Sci.*, vol. 37, no. 1, pp. 7-1–7-28, Jan. 2002.

[25] F. Soulat, "Sea surface remote sensing with GNSS and sunlight reflections," Ph.D. dissertation, Univ. Politecnica Catalunya, Barcelona, Spain, 2003.

[26] A. Komjathy, M. Armatys, D. Masters, P. Axelrad, V. Zavorotny, and S. Katzberg, "Retrieval of ocean surface wind speed and wind direction using reflected GPS signals," *J. Atmos. Ocean. Technol.*, vol. 21, no. 3, pp. 515–526, Mar. 2004.

[27] O. Germain, G. Ruffini, F. Soulat, M. Caparrini, B. Chapron, and P. Silvestrin, "The Eddy experiment: GNSS-R speculometry for directional sea-roughness retrieval from low altitude aircraft," *Geophys. Res. Lett.*, vol. 31, no. 21, pp. L12306-1–L12306-4, Nov. 2004.

[28] S. Gleason, S. Hodgart, S. Yiping, C. Gommenginger, S. Mackin, M. Adjrad, and M. Unwin, "Detection and processing of bistatically reflected GPS signals from low-earth orbit, for the purpose of ocean remote sensing," *IEEE Trans. Geosci. Remote Sens.*, vol. 43, no. 6, pp. 1229–1241, Jun. 2005.

[29] D. Thompson, T. Elfouhaily, and J. Garrison, "An improved geometrical optics model for bistatic GPS scattering from the ocean surface," *IEEE Trans. Geosci. Remote Sens.*, vol. 43, no. 12, pp. 2810–2821, Dec. 2005.

[30] S. T. Gleason, "Remote sensing of ocean, ice and land remote sensing using bistatically scattered GNSS signals from low earth orbit," Ph.D. dissertation, Univ. Surrey, Surrey, U.K., 2006.

[31] S. J. Katzberg, O. Torres, and G. Ganoe, "Calibration of reflected GPS for tropical storm wind speed retrievals," *Geophys. Res. Lett.*, vol. 33, no. 18, pp. L18602-1–L18602-5, Sep. 2006.

[32] J. Marchan-Hernandez, N. Rodriguez-Alvarez, A. Camps, X. Bosch-Lluis, I. Ramos-Perez, and E. Valencia, "Correction of the sea state impact in the L-band brightness temperature by means of delay-Doppler maps of global navigation satellite signals reflected over the sea surface," *IEEE Trans. Geosci. Remote Sens.*, vol. 46, no. 10, pp. 2914–2923, Oct. 2008.

[33] M. Clarizia, C. Gommenginger, S. Gleason, M. Srokosz, C. Galdi, and M. di Bisceglie, "Analysis of GNSS-R delay-Doppler maps from the UK-DMC satellite over the ocean," *Geophys. Res. Lett.*, vol. 36, no. 2, pp. L02608-1–L02608-5, Jan. 2009.

[34] M. Clarizia, C. Gommenginger, M. di Bisceglie, C. Galdi, and M. Srokosz, "Simulation of L-band bistatic returns from the ocean surface: A facet approach with application to ocean GNSS reflectometry," *IEEE Trans. Geosci. Remote Sens.*, vol. 50, no. 3, pp. 960–971, Mar. 2012.

[35] J. Marchan-Hernandez, E. Valencia, N. Rodriguez-Alvarez, I. Ramos-Perez, X. Bosch-Lluis, A. Camps, F. Eugenio, and J. Marcello, "Sea-state determination using GNSS-R data," *IEEE Geosci. Remote Sens. Lett.*, vol. 7, no. 4, pp. 621–625, Oct. 2010.

[36] E. Valencia, A. Camps, J. Marchan-Hernandez, H. Park, X. Bosch-Lluis, N. Rodriguez-Alvarez, and I. Ramos-Perez, "Ocean surfaces scattering coefficient retrieval by delay Doppler map inversion," *IEEE Geosci. Remote Sens. Lett.*, vol. 8, no. 4, pp. 750–754, Jul. 2011.

[37] M. P. Clarizia, "Investigating the effect of ocean waves on ocean-reflected GPS measurements," Ph.D. dissertation, School Ocean Earth Sci., Univ. Southampton, Southampton, U.K., 2012.

[38] S. Gleason, "Space-based GNSS scatterometry: Ocean wind sensing using an empirically calibrated model," *IEEE Trans. Geosci. Remote Sens.*, vol. 51, no. 9, pp. 4853–4863, Sep. 2013.
[39] M. Unwin, S. Gao, R. De Vos Van Steenwijk, P. Jales, M. Maqsood, C. Gommenginger, J. Rose, C. Mitchell, and K. Partington, "Development of low–cost spaceborne multi–frequency GNSS receiver for navigation and GNSS remote sensing," *Int. J. Space Sci. Eng.*, vol. 1, no. 1, pp. 20–50, Jan. 2013.
[40] N. Rodriguez-Alvarez, D. M. Akos, V. U. Zavorotny, J. A. Smith, A. Camps, and C. W. Fairall, "Airborne GNSS-R wind retrievals using delay-Doppler maps," *IEEE Trans. Geosci. Remote Sens.*, vol. 51, no. 1, pp. 626–641, Jan. 2013.
[41] C. Ruf, S. Gleason, Z. Jelenak, S. Katzberg, A. Ridley, R. Rose, J. Scherrer, and V. Zavorotny, "The NASA EV-2 Cyclone Global Navigation Satellite System (CYGNSS) mission," in *Proc. IEEE Aerosp. Conf.*, 2013, pp. 1–7.
[42] C. Ruf, A. Lyons, M. Unwin, J. Dickinson, R. Rose, D. Rose, and M. Vincent, "CYGNSS: Enabling the future of hurricane prediction," *IEEE Geosci. Remote Sens. Mag.*, vol. 1, no. 2, pp. 52–67, Jun. 2013.
[43] M. J. Unwin, S. Gleason, and M. Brennan, "The space GPS reflectometry experiment on the UK disaster monitoring constellation satellite," in *Proc. ION GNSS*, 2003, pp. 1–8.
[44] M. Unwin, P. Blunt, R. van Steenwijk, S. Duncan, G. Martin, and P. Jales, "GNSS remote sensing and technology demonstration on TechDemoSat-1," in *Proc. 24th Int. Tech. Meet. Satellite Div. ION GNSS*, 2011, pp. 2970–2975.
[45] M. Unwin, P. Jales, P. Blunt, S. Duncan, M. Brummitt, and C. Ruf, "The SGR-ReSI and its application for GNSS reflectometry on the NASA EV-2 CYGNSS mission," in *Proc. IEEE Aerosp. Conf.*, 2013, pp. 1–6.
[46] T. Elfouhaily, D. R. Thompson, and L. Linstrom, "Delay-Doppler analysis of bistatically reflected signals from the ocean surface: Theory and application," *IEEE Trans. Geosci. Remote Sens.*, vol. 40, no. 3, pp. 560–573, Mar. 2002.
[47] H. Hersbach, "Comparison of C-band scatterometer CMOD5.N equivalent neutral winds with ECMWF," *J. Atmos. Ocean. Technol.*, vol. 27, no. 4, pp. 721–736, Apr. 2010.
[48] X.-M. Li and S. Lehner, "Algorithm for sea surface wind retrieval from TerraSAR-X and TanDEM-X data," *IEEE Trans. Geosci. Remote Sens.*, vol. 52, no. 5, pp. 2930–2941, May 2014.
[49] D. Allan, "Statistics of atomic frequency standards," *Proc. IEEE*, vol. 54, no. 2, pp. 221–230, Feb. 1966.
[50] G. S. Brown, "The average impulse response of a rough surface and its applications," *IEEE Trans. Antennas Propag.*, vol. AP-25, no. 1, pp. 67–74, Jan. 1977.
[51] E. Samuel-Cahn, "Combining unbiased estimators," *Amer. Stat.*, vol. 48, no. 1, pp. 34–36, Feb. 1994.
[52] National Data Buoy Center. [Online]. Available: www.ndbc.noaa.gov



Maria Paola Clarizia received the M.S. degree in telecommunications engineering (*summa cum laude*) in 2007 from the University of Sannio, Benevento, Italy, and the Ph.D. degree in GNSS-reflectometry from the School of Ocean and Earth Science, University of Southampton, Southampton, U.K.

She has worked as a Research Engineer in the field of SAR altimetry and GNSS-Reflectometry for Starlab Barcelona (SL), and as a Research Scientist in the field of GNSS-Reflectometry for the Natural Environment Research Council (NERC) at the National Oceanography Centre (NOC) in Southampton. In April 2013, she joined the University of Michigan as a Postdoctoral Research Fellow, developing wind speed retrieval algorithms for the NASA CYGNSS mission. Her research interests are in the field of GNSS-Reflectometry, altimetry (conventional, SAR, coastal), GNSS-Radio Occultation, sea surface simulations and electromagnetic scattering models, data analysis and statistical processing.



Christopher S. Ruf (S'85–M'87–SM'92–F'01) received the B.A. degree in physics from Reed College, Portland, OR, USA, and the Ph.D. degree in electrical and computer engineering from the University of Massachusetts at Amherst, MA, USA.

He is currently Professor of atmospheric and space sciences, Professor of electrical engineering, and Director of the Space Physics Research Laboratory at the University of Michigan, Ann Arbor, MI, USA; and Principal Investigator of the Cyclone Global Navigation Satellite System NASA Earth Venture mission. He has worked previously at Intel Corporation, Santa Clara, CA, USA, Hughes Space and Communication, the NASA Jet Propulsion Laboratory, Pasadena, CA, USA, and Penn State University, College Park, PA, USA. His research interests include GNSS-R bistatic scatterometry, microwave radiometry, atmosphere and ocean geophysical retrieval algorithm development, and sensor technology.

Dr. Ruf is a member of the American Geophysical Union (AGU), the American Meteorological Society (AMS), and Commission F of the Union Radio Scientifique Internationale. He is former Editor-in-Chief of the IEEE TRANSACTIONS ON GEOSCIENCE AND REMOTE SENSING and has served on the editorial boards of *Radio Science* and the *Journal of Atmospheric and Oceanic Technology*. He has been the recipient of four NASA Certificates of Recognition and seven NASA Group Achievement Awards, as well as the 1997 TGRS Best Paper Award, the 1999 IEEE Resnik Technical Field Award, and the 2006 IGARSS Best Paper Award.



Philip Jales received the MPhys degree in physics from The University of Manchester, Manchester, U.K., and the Ph.D. degree in 2012 from the University of Surrey, Surrey, U.K., working at the Surrey Space Centre on Spaceborne Receiver Design for Scatterometric GNSS Reflectometry.

He is currently working as a GNSS engineer at Surrey Satellite Technology Ltd (SSTL) on the CYGNSS mission. Previous to this he has worked on electro-optical instruments for aerosol characterization at the Defense Science and Technology Laboratory (DSTL) in U.K.



Christine Gommenginger received a Diplome dEtudes Approfondies in electromagnetics, telecommunications and remote-sensing from the University of Toulon, La Garde, France-University of Nice Sophia Antipolis, Nice, France, followed by the Ph.D. degree in microwave radar remote sensing of ocean surface roughness at low grazing angles from the University of Southampton, Southampton, U.K.

She has worked at the National Oceanography Centre for over 15 years. Her interests are wide-ranging and include active and passive microwave remote sensing of the ocean, understanding interactions of microwave signals with the ocean surface, remote sensing of ocean wind and waves and new Earth Observation technologies. Her recent work includes research in along-track interferometric SAR, GNSS Reflectometry, SAR altimetry, salinity from space and wide-swath ocean altimetry.